Conducting mechanism in the epitaxial *p*-type transparent conducting oxide Cr_2O_3:Mg

L. Farrell,* K. Fleischer, D. Caffrey, D. Mullarkey, E. Norton, and I. V. Shvets
School of Physics and Centre for Research on Adaptive Nanostructures and Nanodevices (CRANN), Trinity College, University of Dublin, Dublin 2, Ireland

(Received 10 October 2014; revised manuscript received 4 February 2015; published 2 March 2015)

Epitaxial *p*-type transparent conducting oxide (TCO) Cr_2O_3:Mg was grown by electron-beam evaporation in a molecular beam epitaxy system on *c*-plane sapphire. The influence of Mg dopants and the oxygen partial pressure were investigated by thermoelectric and electrical measurements. The conduction mechanism is analyzed using the small-polaron hopping model, and hopping activation energies have been determined, which vary with doping concentration in the range of 210–300 ± 5 meV. Films with better conductivity were obtained by postannealing. The effect of postannealing is discussed in terms of a crystallographic reordering of the Mg dopant. The highest Seebeck mobilities obtained from thermoelectric measurements are of the order of 10^{-4} $cm^2V^{-1}s^{-1}$. We investigate the fundamental properties of a Mg dopant in a high crystalline quality epitaxial film of a binary oxide, helping us understand the role of short range crystallographic order in a *p*-type TCO in detail.

DOI: 10.1103/PhysRevB.91.125202 PACS number(s): 71.20.Be, 71.38.Ht, 72.80.Ga, 73.50.Lw

I. INTRODUCTION

Transparent conducting oxides (TCOs) are a material class used in flat screen displays, organic light emitting diodes, and thin film solar cells. Current hole conducting TCOs (*p*-type) still suffer severely from lower transparencies and conductivities in comparison to *n*-type TCOs, which limits their applicability in devices [1]. The ultimate goal of using *p*-type TCOs as active layers in the so-called invisible circuit still remains unrealized [2]. A transparent *p*-*n* junction could be used to make fully transparent optoelectronics devices (transparent electronics) and blue or ultraviolet (UV) light emitting diodes [1,3].

The delafossite *p*-type TCO $CuAlO_2$ was first investigated in 1997 and accelerated research in the field of TCOs [4]. In these materials, the fully occupied Cu 3*d* states hybridize with the O 2*p* states at the valence band to create a more dispersed valence band maximum. This allows for less localized holes and, due to the occupied nature of the Cu 3*d* states, large bandgaps and optical transparency [5]. These materials include, but are not limited to, $CuGaO_2$ [6], $CuScO_2$ [7], $CuBO_2$ [8], and $CuCrO_2$ [9]. However Cu-delafossites have proven to be hindered by their small-polaron hopping (SPH) mechanism, high deposition temperature, and, in some cases, interband transitions limiting their transparency [10]. Spinel *p*-type TCOs such as $ZnRh_2O_4$, despite the advantage of retaining their conductivity as amorphous thin films, have relatively low conductivity [11] (0.1 Scm^{-1}). Similarly the distorted delafossite $SrCu_2O_2$ also has low conductivity [12] (0.053 Scm^{-1}). These are not ideal conductivities for a *p*-type TCO, as in comparison *n*-type TCOs can possess conductivities as high as 10^4 Scm^{-1}. Oxychalcogenides are a promising class of *p*-type TCOs, which display greater mobility than the Cu-delafossites while maintaining wide bandgaps. Oxychalcogenides consist of layered $[M_2O_2]^{2+}$ and $[Cu_2Ch_2]^{2-}$ blocks, where M represents a 3^+ cation, typically La or Ba, and Ch represents one of the Chalcogenides such as S, Se, Te. The bandgap has been shown to decrease for the larger atomic radii of Se and Te, with a corresponding increase in conductivity [13]. Thus an appropriate chemical selection to tune the properties of these materials could result in high conductivity *p*-type TCOs. Cr_2O_3 is considered here as a candidate *p*-type TCO. This material has *p*-type conductivity, and its electronic properties are significantly improved when it is simultaneously doped with Mg and N [14]. A binary oxide such as Cr_2O_3 is relatively easy to fabricate in comparison to layered materials. The possibility of using dopants to create a *p*-*n* homojunction with Cr_2O_3 has motivated our research.

Even though *p*-type TCOs still lack in performance, they have been employed as hole injecting layers [15–17]. In particular, Cr_2O_3 and Cr_2O_3:N have received attention as buffer layers in organic solar cells [18,19]. Stoichiometric Cr_2O_3 is usually regarded as an insulator, although there are reports of very low native *p*-type conductivity [20,21]. For our high quality epitaxial films, no native *p*-type conductivity was present. Doping with Mg [22–26], Ni [23,26,27], and Li [26,28] are known to induce *p*-type conductivity in Cr_2O_3, also co-doping with Mg and N has been reported [14]. In comparison to the polycrystalline material discussed in these studies, epitaxial films are expected to show improved electrical and optical properties due to a significantly reduced number of defects and grain boundaries. In this study, molecular beam epitaxy (MBE) was used to grow high quality Cr_2O_3 with controlled Mg doping. There is uncertainty in the literature over the exact conduction mechanism in Cr_2O_3. Band conduction [29], SPH [21], and variable range hopping [30] have been suggested. Indeed, it is heavily discussed in the literature what model is applicable for *p*-type TCOs. [31] To fully distinguish whether the SPH model is appropriate, high temperature measurements of conductivity and thermopower are typically analyzed to ascertain whether an activated mobility exists [32]. This alone is not enough to distinguish the mechanism definitively without an understanding of the effective density of states [33]. In the absence of density functional theory (DFT) we cannot perform such an analysis. Further work is required to exclude the possibility that epitaxial Cr_2O_3:Mg is a band conductor. In this paper we provide evidence that suggests that the SPH mechanism is applicable for epitaxial Cr_2O_3:Mg over the temperature range considered. Unlike the familiar

*lefarrel@tcd.ie

broad-band conduction model where carriers are excited into nonlocalized energy states, in the SPH model, carriers are localized due to strong electron-phonon interactions and are trapped in potential wells. The carriers move by "hopping" to available sites. Small polaron conduction is unfavorable for a *p*-type TCO as they are usually associated with high carrier concentrations ($>10^{21}$ cm^{-3}) [11] and correspondingly low mobilities. The present paper allows us to verify the conduction mechanism in a less complex binary oxide system, to understand the microscopic charge transport mechanism, and to outline paths to increase the mobility in the material. This paper also provides a basis to understand and improve other related but more complicated ternary *p*-type TCOs such as delafossites and oxychalcogenides.

II. EXPERIMENTAL DETAILS

Cr_2O_3 (0001) films were grown epitaxially using a DCA M600 MBE with a base pressure of 1.3×10^{-7} Pa. Samples were grown on single-side polished (0001) Al_2O_3 substrates from MTI Corporation. The substrates were chemically cleaned and then annealed *in situ* at 873 K, 1.7×10^{-3} Pa oxygen partial pressure, for 2 h prior to deposition. Cr metal or Cr_2O_3 pieces were e-beam evaporated at an oxygen partial pressure (varied between 1.3×10^{-4} and 5.3×10^{-3} Pa) with the substrate temperature maintained at 873 K. The growth rate was approximately 0.2 Å/s. The doping was achieved by controlling the supplied power to a second e-beam evaporator loaded with MgO. The materials used in this study for the growth were Cr pieces (99.998% purity), Cr_2O_3 pieces (99.9% purity), and MgO pellets (99.95%), all supplied by Kurt J. Lesker Company. An INFICON IC/5 deposition rate controller is used in conjunction with crystal monitors to control the growth rate for each electron beam evaporator. The crystal monitors were calibrated by comparing the actual thickness of deposited films by x-ray reflectivity (XRR). In order to quantify the Mg dopant concentration, x-ray photoemission spectroscopy (XPS) measurements were performed on a VG Scientific ESCAlab MKII system using Al Kα x-rays (1486.7 eV). The ratio of the Mg 2*s* peak to the Cr 3*s* peak was used as an indication of the Mg doping concentration.

The crystalline quality of the films was assessed by x-ray diffraction (XRD) measurements using a Bruker D8 Advance diffractometer using a Cu Kα source with a double bounce Ge monochromator. Symmetric ω-2θ scans were performed around the substrate peak (0001) of sapphire (41.676°). For selected samples, lamellae for transmission electron microscopy (TEM) were prepared using an FEI Strata focused-ion beam (FIB). Final low kilovolt (2–5 kV) thinning was also done using a Carl Zeiss Auriga FIB. TEM imaging was performed using an FEI Titan operating at 300 kV. To complement the crystallographic information, the A_{1g} vibrational mode was measured by micro-Raman spectroscopy in a Renishaw InVia system using a 488 nm Ar ion laser in backscattering geometry. To highlight the effect on the A_{1g} mode, only differential measurements are shown where measurements in $z(x,x)\bar{z}$ and $z(x,y)\bar{z}$ geometry have been subtracted to remove the fluorescent background as well as the substrate and Cr_2O_3 related modes with E_g symmetry. The total UV-visible (UV-Vis) transmittance and reflectance of the films were measured with a Perkin Elmer 650S spectrophotometer equipped with an integrating sphere and operating in the wavelength range from 200 to 850 nm. All measurements were performed including the sapphire substrate with air as a reference. Postannealing of samples was performed in a furnace in the presence of 1×10^5 Pa of oxygen for 2 h at a temperature of 973 K. Electrical conductivity measurements were performed on the samples using a linear four point probe geometry with gold coated tips. The temperature was varied from 300 to 450 K during electrical measurements. Seebeck measurements confirmed the *p*-type nature of the films. These measurements were performed using a homebuilt system, which varied the temperature gradient from 1 to 10 K across the sample while measuring the potential difference. This gave us an estimate of the Seebeck coefficient in the 293 to 308 K range. The sample was clamped between two sets of copper blocks: one at the cold side and the other at the hot side. The set of blocks on the cold side sat on electrically insulating heat exchange foil over a metal block that acted as a heat sink. The set of blocks on the hot side sat on a ceramic heater. The supplied heater power was controlled using a proportional-integral-derivative (PID) controller, while the actual temperature at either end of the sample was measured using a Type K thermocouple (chromel vs alumel) thermally connected but electrically isolated from the copper block. The measurements were taken in a vacuum of approximately 200 Pa. The potential difference was measured using an Agilent 34401A Multimeter. The contribution of the Cu connection to the Seebeck coefficient (1.5 μV/K) was subtracted from the obtained values.

III. STRUCTURAL CHARACTERIZATION

Cr_2O_3 with the mineral name eskolaite is an antiferromagnetic insulator with a Néel temperature $T_N = 307$ K [34]. Cr_2O_3 is the most stable form of this durable oxide [35]. Cr_2O_3 adopts the corundum structure where oxygen atoms form a hexagonal close-packed structure. The Cr atoms occupy two-thirds of the interstitial octahedral sites [36,37]. The primitive cell is rhombohedral, while the unit cell is hexagonal with lattice parameters of $a = 0.4958$ nm and $c = 1.3594$ nm [see Fig. 1(a)]. The lattice parameters of Al_2O_3 are $a = 0.4759$ nm and $c = 1.2992$ nm. Figure 1(b) displays a TEM image of a cross section of an epitaxial Cr_2O_3 (0001) film showing a well-ordered thin film with a few stacking faults at the interface to relieve mismatch induced strain.

All samples were analyzed by XRD *ex situ*. Some representative data are shown in Fig. 2. As the films grew epitaxially on the *c* plane of sapphire, only the (006) hexagonal *c* plane peak of the Cr_2O_3 film and its higher order (0012) reflex were observed. Due to the large in-plane lattice mismatch between the film and the substrate (4.2%), the films grew in a relaxed manner, as previously reported [38]. Films as thin as 20 nm are already fully relaxed. This was confirmed from the in-plane lattice parameter measured by reciprocal space mapping (RSM) (see Fig. 3). For highly doped films (>10%), a tetragonal distortion of the crystal structure was observed with resulting larger *c* lattice parameters, as determined from the ω-2θ XRD scans. This is possibly a shift to the spinel $MgCr_2O_4$ phase, as reported before [25]. The XRR measurements were used to determine the thickness of each individual film to

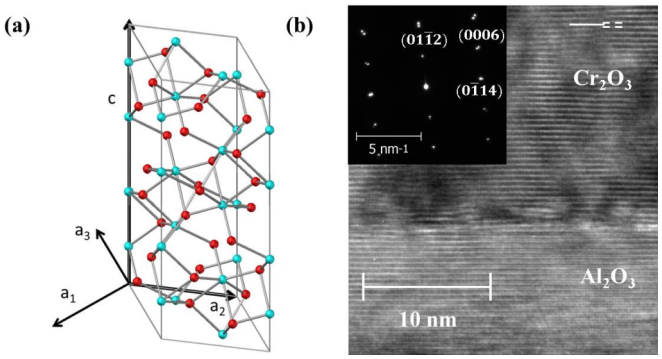

FIG. 1. (Color online) (a) Hexagonal unit cell of Cr_2O_3 with the *a* and *c* lattice directions indicated. Red spheres indicate O atoms, while the cyan spheres are Cr atoms. (b) TEM image of epitaxial Cr_2O_3 (0001) along the $[2\bar{1}\bar{1}0]$ zone axis. A misfit dislocation is highlighted in the top right corner. The inset shows a selected area electron diffraction pattern where the orientation of the film can be seen clearly.

calculate the conductivity of the material from the measured sheet resistance. A number of thin film samples ranging from 20 to 150 nm in thickness and grown at different conditions were investigated.

The effects of postannealing on the *c* and *a* lattice parameter of Cr_2O_3 were investigated by XRD and RSM. A minor shift of the 2θ value in the XRD pattern is visible in Fig. 2. This corresponds to a decrease in the *c* lattice parameter. This effect is not significant, and we do not believe these changes affect the conductivity mechanism.

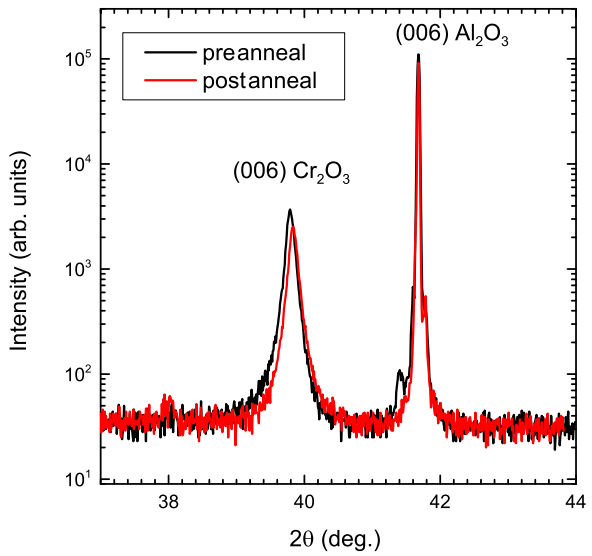

FIG. 2. (Color online) XRD pattern of 120 nm thick Cr_2O_3 film on sapphire. The effect of postannealing is compared, and only a minor shift in the 2θ reflex of Cr_2O_3 (006) is observed. Note the small peak near the sapphire main reflex. This is due to the mosaicity of the substrate.

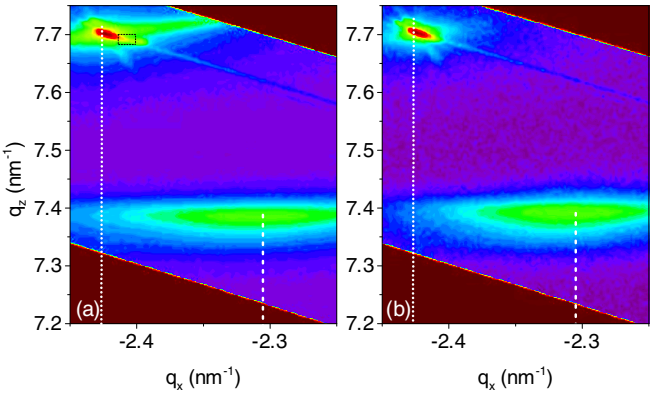

FIG. 3. (Color online) RSM for a pre- (a) and postannealed (b) sample with 120 nm thickness. No major changes are evident, and the films grow in a relaxed manner, as indicated by the displacement of the substrate and film peaks. The q_x value corresponding to the sapphire *a* lattice parameter is shown with the white dotted line. There is some mosaicity in (a), highlighted by the dashed rectangle that generates the additional small peaks to the lower right of the sapphire reflex. This was also present in the out-of-plane scan (see Fig. 2).

IV. ELECTRICAL CHARACTERIZATION

Previously, ac impedance spectroscopy has been used to estimate the contribution of grain boundaries to the bulk electrical conductivity [31,39,40]. However, this is not investigated here as the difference is expected to be small due to the low number of such defects in epitaxial samples. Room temperature conductivity data are shown in Fig. 4 as a function

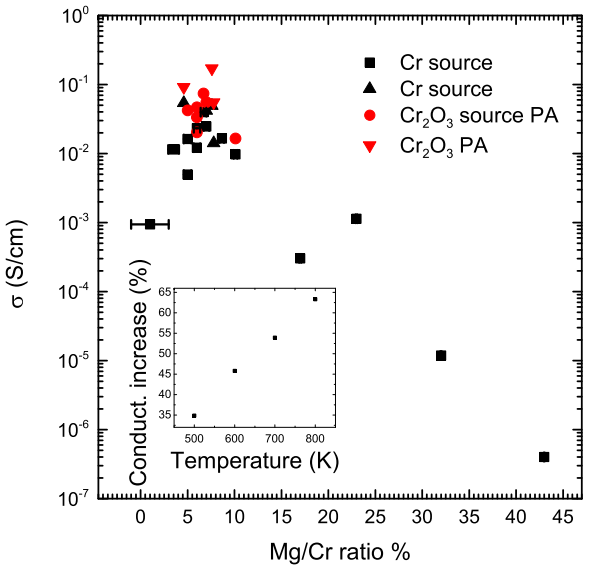

FIG. 4. (Color online) Conductivity vs Mg/Cr ratio. The inset shows the conductivity increase with postannealing temperature for a two hour anneal in oxygen. The preanneal Mg/Cr ratio was 4% for these samples. Square symbols (■) represent samples grown from the Cr metal source, while triangles (▲) indicate those grown from the ceramic Cr_2O_3 source. Circles (●) indicate Cr metal source samples postannealed, and inverted triangles (▼) are postannealed samples grown from the ceramic Cr_2O_3 source.

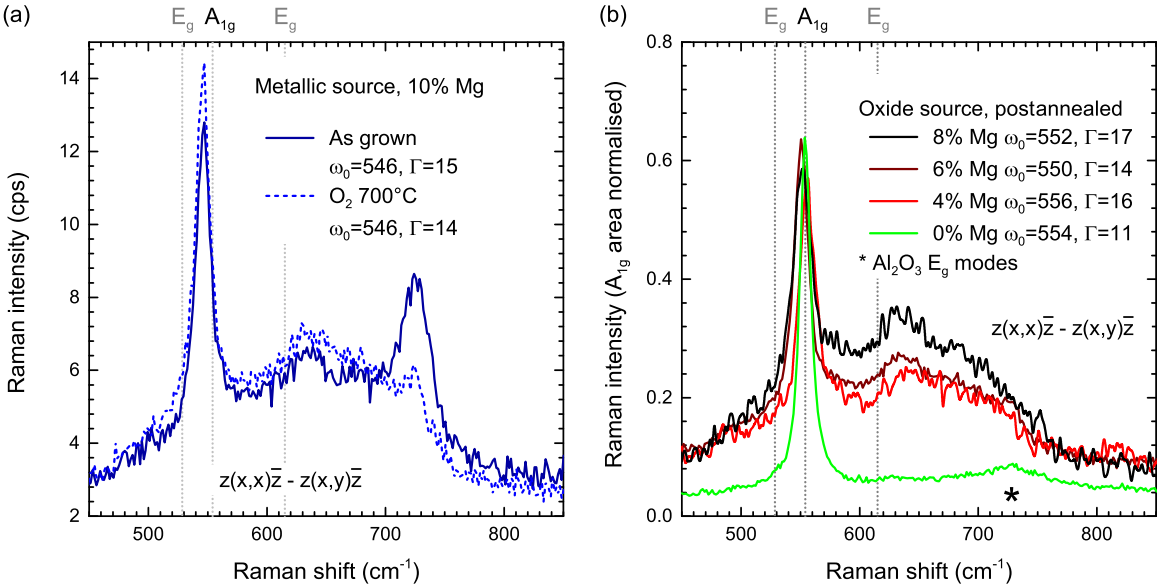

FIG. 5. (Color online) (a) Raman spectra of a sample grown from metallic Cr before and after postannealing. The reduction in the Mg induced LVM around 720 cm^{-1} following the anneal is attributed to the redistribution of Mg in the Cr_2O_3 lattice. (b) Raman spectra of postannealed samples grown from an oxide source with increasing Mg concentration showing the increase in Mg induced broad band defect structures. For better comparison, the signal was normalized to the area of the $Cr_2O_3 A_{1g}$ mode. The dotted lines represent the E_g and A_{1g} Raman modes for stoichiometric bulk Cr_2O_3.

of the Mg/Cr ratio. Films without Mg doping are insulating, suggesting no significant density of intrinsic, electrically active defects. Once a small amount of Mg is present, the conductivity increases significantly. Most likely the Mg atoms are replacing Cr atoms during growth of the Cr_2O_3 film. As the valency of Cr is in the 3^+ state, Mg substitution (2^+ valency) leads to hole formation. This can be represented using Kröger-Vink notation $Mg^{\bullet}_{Cr}$. Mg concentration in the range 5–10% gives the most conductive films. Higher concentrations lead to more resistive films.

Films grown from a Cr metal source have room temperature conductivity in the 0.017–0.025 S/cm range. When grown from the ceramic Cr_2O_3 source, the film's conductivity is significantly higher, in the 0.03–0.05 S/cm range. This is most likely due to increased oxygen content during growth, as discussed below. The most conductive films (~0.17 S/cm) have conductivity of the same order of magnitude as spray pyrolysis grown samples from a previous report (~0.33 S/cm) [14]. However, this was only achieved after postannealing in 1×10^5 Pa oxygen pressure at 973 K for 2 h. Cu delafossites have conductivities that range from 0.025 Scm^{-1} for $CuYO_2$ to 0.36 Scm^{-1} for $CuAlO_2$ and as high as 220 Scm^{-1} for $CuCr_{0.95}Mg_{0.05}O_2$ films [9,41,42]. Therefore, MBE grown Cr_2O_3:Mg films have relatively low conductivity in comparison. The inset of Fig. 4 shows the conductivity increase as a function of the postannealing process temperature for four samples grown simultaneously. These films have a Mg/Cr ratio of 4% prior to postannealing. The higher temperatures result in more conductive films. We attribute this to a homogenization of the Mg within the sample.

High temperature diffusion of the Mg is an important factor in achieving conductive samples. Raman spectra of as grown samples show a characteristic local vibrational mode (LVM) in A_{1g} symmetry developing at 720 cm^{-1} with increasing Mg concentration (see Fig. 5). This phonon mode is consistent with highly pressurized (15 GPa) nanoscale inclusions of $MgCr_2O_4$ [43]. For such a coherent phonon mode, typically 5–10 adjacent unit cells with similar coordination are required. After postannealing, the Mg related LVM is dramatically reduced, consistent with a more homogenous spread of $Mg^{\bullet}_{Cr}$ defects throughout the film and a reduction of the number of Mg rich $MgCr_2O_4$ nanoinclusions. At the same time, a broad range defect induced Raman structure remains. The latter is consistent with the appearance of either more random Mg-O related modes, a defect induced breakdown of Raman selection rules leading to a signal from otherwise Raman forbidden infrared (IR) active Cr_2O_3 modes, or distortions in the oxygen octahedral or Cr atomic positions. The most conductive samples show a particularly strong broad Raman mode with a related reduction in the Cr_2O_3 A_{1g} mode around 545 cm^{-1}. This mode should occur at 553−555 cm^{-1} for stoichiometric bulk Cr_2O_3. This peak is always shifted to lower wave numbers, indicative of a Mg induced lattice expansion due to tensile strain and/or disorder [44–46]. This behavior is again consistent with more equally spread $Mg^{\bullet}_{Cr}$ defects and an increase in the defect induced distortion of the Cr-O octahedral.

It was possible to improve the conductivity of the films by growing the films in higher oxygen partial pressure (see Fig. 6). This dependency is consistent with many findings for *p*-type oxides, where a suppression of compensating defects such as oxygen vacancies V_O or an increase in hole creating oxygen interstitials O_i leads to improved conductivity [25]. Although Cr_2O_3 is known as an oxygen excess oxide [24,30], suggesting oxygen interstitial formation, we do not believe that these defects make a significant contribution to the conductivity. The solubility of MgO in Cr_2O_3 is related to the oxygen partial pressure and the growth temperature [47]. It is likely that

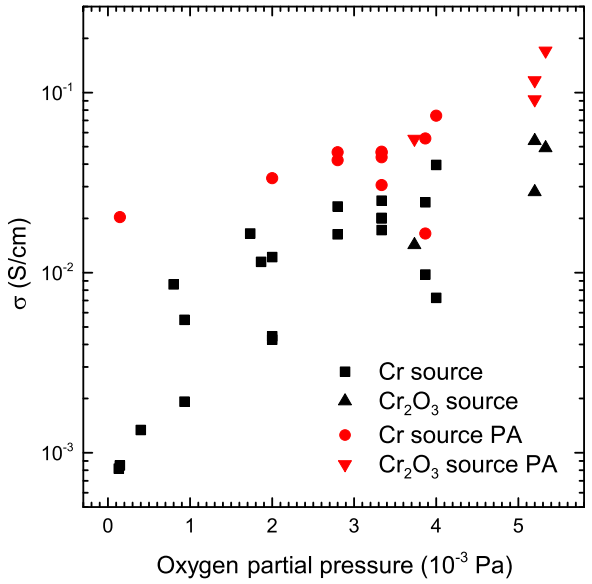

FIG. 6. (Color online) Conductivity (at room temperature) vs oxygen partial pressure. Samples shown are in the optimum doping range of 5–10%. Square symbols (■) represent samples grown from the Cr metal source, while triangles (▲) indicate those grown from the ceramic Cr_2O_3 source. Circles (●) indicate Cr metal source samples postannealed, and inverted triangles (▼) are postannealed samples grown from the ceramic Cr_2O_3 source.

the redistribution of Mg dopants is the most dominant effect as oxygen vacancies are not predicted to be readily formed [48] and oxygen interstitials are predicted to be electrically inactive. Thus the oxygen pressure dependence in Fig. 6 is representative of greater dopant solubility. Mixed valency of the Cr ions ($Cr^{3+} \rightarrow Cr^{4+}$) could also be responsible for charge compensation [23,49], which would reduce the number of holes. However, as the oxygen partial pressure in MBE is substantially lower than for atmospheric growth techniques such as spray pyrolysis, we do not observe any brown discoloration that has been attributed to Cr^{4+} or Cr^{6+} formation [50]. Native p- and n-type defects such as V_{Cr} and Cr_i could be responsible for charge carriers, as previously theorized [48]; however, no native conductivity was present in undoped samples. Therefore, we expect this effect to be negligible. In many other p-type oxides and nitrides, hydrogen interstitials, H_i, have been proven to be detrimental due to their compensating nature [51–53]. However, for MBE-grown Cr_2O_3, residual hydrogen levels are expected to be low, and we do not expect H_i to have a significant impact on the conductivity of the films.

V. SPH IN Cr_2O_3

SPH typically occurs in mixed-valence transition metal oxides where the electron-lattice interaction is strong [39,54,55]. Unlike in the free electron model, charge is localized to the lattice, or polarized. This prevents the charge from moving freely through the material. Initial Hall mobility measurements had shown that the mobility is below the experimental limit of our Hall setup ($\sim 0.1\,cm^2V^{-1}s^{-1}$). If the mobility lies below the Bosman and van Daal limit [33] ($\mu < 0.1\,cm^2V^{-1}s^{-1}$), it is likely that electrical transport follows the SPH model. The band conductor model has been previously used to estimate mobility [29]. Single crystal growth was suggested to determine whether a Hall voltage can be extracted as no signal was detected in their measurements. We are also unable to detect a Hall voltage and believe this is at odds with the anticipated mobility a band conductor would exhibit. Considering the Arrhenius activation energy obtained from fitting the electrical data (see Fig. 7), we obtain a value of 200 ± 5 meV for a sample with 8% Mg doping. The total number of Cr sites are $N = 4.15 \times 10^{22}\,cm^{-3}$, which corresponds to $3.3 \times 10^{21}\,cm^{-3}$ carrier sites for this 8% sample. Using the Arrhenius equation to calculate the total number of activated carriers at room temperature, we obtain $1.3 \times 10^{18}\,cm^{-3}$. The corresponding mobility is then expected to be $0.4\,cm^2V^{-1}s^{-1}$, which is above the experimental limit of our Hall setup. Thus the SPH model is used to fit the temperature dependence of conductivity. The question of whether the adiabatic or nonadiabatic model is appropriate can be addressed using the Holstein relation [56]. The tunneling probability is deemed to be approximately zero as the overlap integral J is greater than H, where H is calculated as ~0.012 eV using Eq. (1),

$$H = \left(\frac{2k_BTW}{\pi}\right)^{1/4}\left(\frac{h\nu_{ph}}{\pi}\right)^{1/2}. \quad (1)$$

W is the hopping activation energy, ν_{ph} is the phonon frequency, and both are discussed in more detail below. k_B is Boltzmann's constant, and h is Planck's constant. J is estimated as ~0.018 eV using the following approximate expression at 300 K [56],

$$J = 0.67h\nu_{ph}\left(\frac{T}{\theta_D}\right)^{1/4}, \quad (2)$$

where θ_B is the Debye temperature discussed below. As J is greater than H, there should be negligible tunneling probability, and in this case the adiabatic model is appropriate. The SPH conductivity (σ) in the adiabatic case can be expressed by

$$\sigma = \frac{g\nu_{ph}Ne^2a^2c(1-c)}{k_BT}\exp\left(\frac{-W}{k_BT}\right), \quad (3)$$

where g is a geometric factor, N is the density of conducting sites, a is the jump distance between equivalent sites, c is the fraction of occupied carrier sites, and e and k_B are electric charge and Boltzmann's constant. ν_{ph} and W are already defined. Using Eq. (3), the conductivity data can be fitted to obtain the hopping activation energy (see Fig. 8). In our measurements the temperature was varied from 300 to 450 K. Obtained W values range from 210–300 ± 5 meV, in line with previous reports of ~250 meV for nonstoichiometric Cr_2O_3 [21,30]. Equation (3) is valid once the hopping activation energy is the dominant, limiting term in the conduction. Due to a lack of *ab initio* calculations, the energy level of the Mg dopant is not known yet. To assess whether the measured carrier activation is limited by the acceptor activation energy E_a or the hopping activation energy W, we analyzed the temperature dependence of the activation energy with increasing Mg content (see Fig. 7) and the conductivity

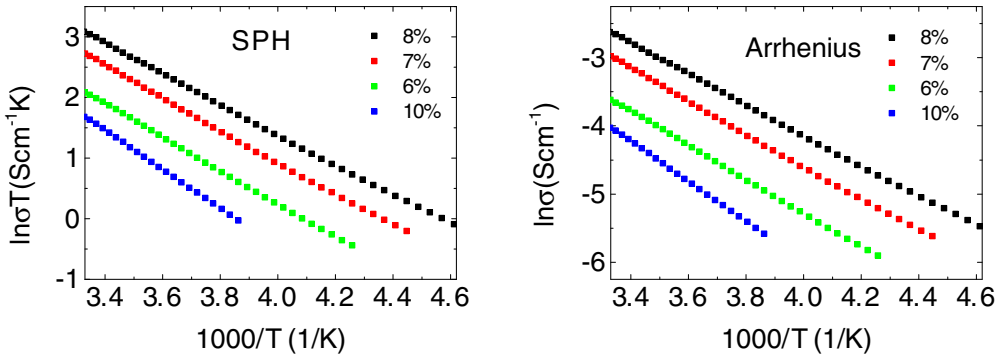

FIG. 7. (Color online) The conductivity was measured as a function of temperature for postannealed samples with different doping concentration (6–10%) over the 300–200 K temperature range. Both the SPH model and Arrhenius model are plotted.

over a larger temperature range. No significant deviation from a single exponential behavior was found in the latter, and the measured activation energy begins to decrease even for low Mg concentration. This suggests that there is only one dominant activation mechanism. A previous paper for undoped Cr_2O_3 also found no significant dependence of the Seebeck coefficient on temperature up to 450 K [30], which is supported by our data on Seebeck measurements with a higher temperature differential (see Fig. 9 inset). This suggests that E_a is significantly smaller than W, and the conductivity is dominated by SPH. The conductivity increase with increasing Mg concentration is then likely a combination of an increase in the number of Cr sites occupied by a polaron due to the doping, combined with a decrease in the hopping activation energy W. The latter is expected due to the increased spatial overlap of polarons at an increased number of occupied sites [49].

An additional indication of SPH is to assess the value for ν_{ph}. The basal plane distance of Cr-Cr atoms is used for the hopping distance $a = 2.94$ Å [57], the geometric factor is taken as $g = 2/6$, and N and c values obtained from thermoelectric measurements are used. Calculated values for ν_{ph} are found in the $2-3 \times 10^{12}$ Hz range ($70-100$ cm^{-1}), which is reasonable for oxide materials and compares well with the first maximum in the expected phonon density of states for Cr_2O_3 of 6×10^{12} Hz (~ 200 cm^{-1}) [58]. This value can be used to estimate the optical Debye temperature $\Theta_D = \hbar\omega/k$, resulting in a value of approximately 120 K. SPH should dominate above $\Theta_D/2 \sim 60$ K. All these considerations are consistent with the SPH mechanism.

In the case of Mg^{2+} acceptor doping, the conductivity is arising from hole creation when Mg atoms replace Cr sites. To a first approximation, the ratio of occupied to available hopping sites c can be expressed as the following ratio:

$$c = \frac{[Mg^{2+}]}{[Mg^{2+}] + [Cr^{3+}]}. \quad (4)$$

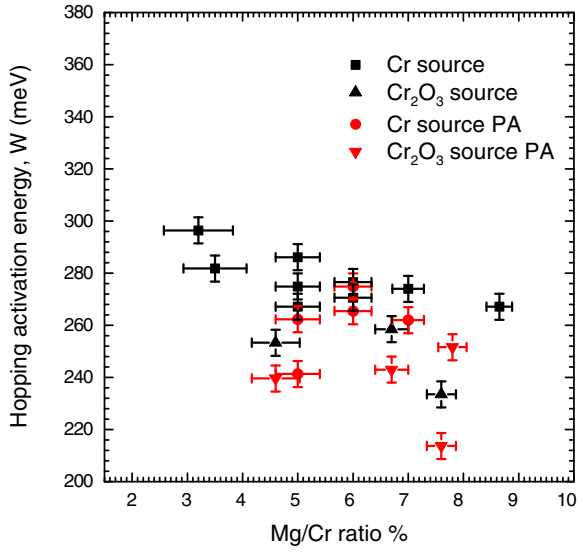

FIG. 8. (Color online) The decrease in W with increasing Mg concentration as determined by XPS. Square symbols (■) represent samples grown from the Cr metal source, while triangles (▲) indicate those grown from the ceramic Cr_2O_3 source. Circles (●) indicate Cr metal source samples postannealed, and inverted triangles (▼) are postannealed samples grown from the ceramic Cr_2O_3 source.

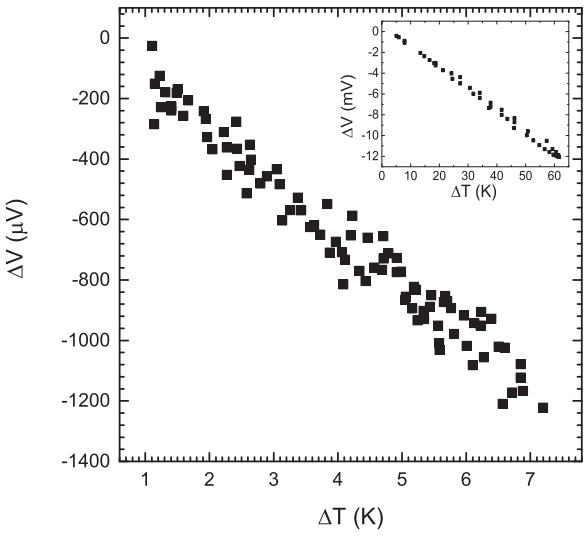

FIG. 9. Representative data of the Seebeck voltage as a function of temperature gradient ΔT. The negative slope indicates a positive Seebeck coefficient. Inset shows a Seebeck voltage over a large ΔT. The Seebeck coefficient was determined by linear fits using $S = -\Delta V/\Delta T$.

This implies that every Cr site is a potential hopping site and that every Mg substitution creates one hole and hence occupied hopping site. For SPH material, the ratio c given by Eq. (4) is closely linked to the thermoelectric properties of the material. Figure 9 shows demonstrative thermoelectric data using a temperature gradient ΔT (1 to 10 K) across the sample of size 10 mm. The temperature gradient induces a hot side and a cold side of the sample. The voltage difference ($\Delta V = V_{\mathrm{Hot}} - V_{\mathrm{Cold}}$) is measured for heating and cooling cycles. The Seebeck coefficient (S) is then the ratio of the voltage difference to the temperature gradient obtained from a linear fit of the data using Eq. (5),

$$S = -\frac{\Delta V}{\Delta T} = -\frac{(V_{\mathrm{Hot}} - V_{\mathrm{Cold}})}{T_{\mathrm{Hot}} - T_{\mathrm{Cold}}}. \tag{5}$$

This avoids any unwanted voltage offset effects [59]. We expect the Seebeck coefficient to be independent of temperature as this is typical for small polaron behavior [41] and has been previously seen in undoped Cr_2O_3 [30]. The sample temperature during measurement is in the range 293 to 308 K. Typical Seebeck coefficients are positive, indicating p-type conduction, and for the most conductive films are $150 \pm 10 \mu \mathrm{VK}^{-1}$. This is similar to Mg doped $CuCrO_2$ [9]. The Seebeck coefficient can be used as a direct measure of the fraction of occupied carrier sites, c, using Eq. (6),

$$S = \pm \frac{k_B}{e} \ln\left[\frac{2(1-c)}{c}\right], \tag{6}$$

where k_B, e, and c have the same definitions as above. It is possible to compare the expected c values from the Mg/Cr ratios with those experimentally determined via the Seebeck coefficient. Measured c values range from 0.05–0.3 and were around two to three times larger than expected for the nominal Mg/Cr ratio. This is unusual as substitutional Mg^{2+} should only generate one charge carrier per substitution. However, the expected values are based on a very simple assumption of the number of potential available hopping sites and also assuming that a homogeneous Mg distribution does not affect the Cr coordination. For highly doped material, dephasing or the presence of compensating defects reduces the total number of available hopping sites, and a larger c is possible. A similar unusually high c has been reported for other p-type TCOs such as Mg doped $CuCrO_2$ [9]. In general we found that during postannealing, where we homogenize the Mg distribution and reduce the number of oxygen vacancies, c values were shown to be reduced compared to the as grown case.

To assess the suitability of a p-type TCO for different electronic devices, the carrier mobility is an important parameter. Hall measurements were performed in a physical property measurement system with field sweeps up to 14 T. However, it was not possible to extract a meaningful value for the Hall coefficient due to the thermal instability being greater than the signal. Using the thermoelectric measurements, it is possible to estimate the Seebeck mobility of thin films [11,33,41,49,60].

Within the SPH model, c is related to the carrier concentration p by $p = Nc$, where the density of conducting sites N can be calculated using the unit cell volume of the Cr_2O_3 crystal and the number of Cr atoms per unit cell. For the hexagonal representation, there are 12 Cr atoms in a unit cell volume of 2.89×10^{-22} cm^3, which corresponds to

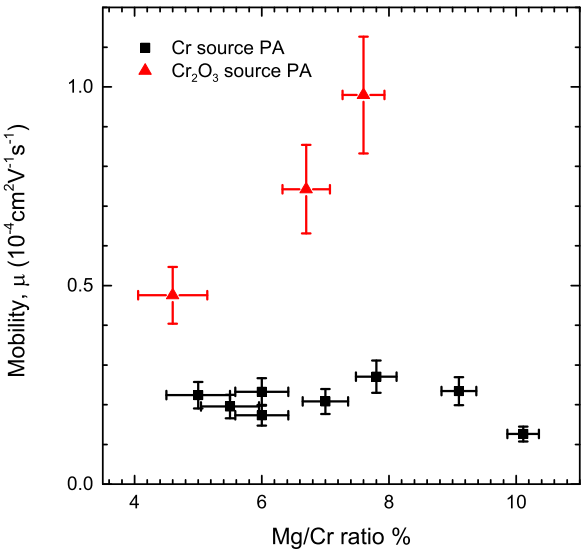

FIG. 10. (Color online) Seebeck mobility as a function of Mg/Cr ratio. Squares (■) indicate Cr metal source samples postannealed, and triangles (▲) are postannealed samples grown from the ceramic Cr_2O_3 source. Higher mobility was observed for the Cr_2O_3 samples.

$N = 4.15 \times 10^{22}$ cm^{-3}. Using the measured conductivity and c values, the Seebeck mobility can be expressed as

$$\mu = \frac{\sigma}{pe} = \frac{\sigma}{Nce}. \tag{7}$$

This assumes a negligible concentration of n-type charge carriers. Figure 10 shows the Seebeck mobility calculated from the Seebeck coefficient as a function of Mg concentration. Only the highest conductivity samples were measured. There is a peak in mobility for the Cr source samples around 8%. The samples grown from the Cr_2O_3 source indicated in red also show a peak at this Mg/Cr ratio and generally exhibited higher mobilities. These mobility values are taken as an order of magnitude indication for room temperature. However, our Seebeck mobilities appear to be at best 1×10^{-4} cm^{2}V^{-1}s^{-1}, which is understandable for SPH but rather small for application purposes. In the case that N is overestimated, as not every Cr site is an available hopping site, then the model is underestimating the mobility.

It is possible to obtain an upper limit on the mobility in materials exhibiting the SPH mechanism [61]. Using the Einstein relation and a diffusion coefficient of $D = a^2/2\tau$, the mobility μ_d is given by

$$\mu_d = \frac{eD}{k_B T} = \frac{ea^2}{2\tau k_B T}, \tag{8}$$

where τ is the time taken for a charge carrier to hop from one site to the next and the other symbols have their usual meaning or are defined previously. For the case of self-trapping the time for phonon induced transitions of the localized charged carrier from ion to ion τ takes considerably longer than the time period of a lattice vibration τ_0. In this condition, the mobility can be expressed as

$$\mu_d < \frac{ea^2}{2\tau_0 k_B T} = \frac{ea^2 \nu_{ph}}{2k_B T}, \tag{9}$$

where ν_{ph} is the phonon frequency corresponding to a lattice vibration. Specifically for Cr_2O_3, the room temperature mobility can be estimated as being much less than 0.04 $cm^2V^{-1}s^{-1}$, using $\nu_{ph} = 2.5 \times 10^{12}$ Hz and $a = 0.294$ nm for the basal plane Cr to Cr distance. This fits reasonably with our results. A theoretical study of the charge transport in Cr_2O_3 used the adiabatic SPH model for both hole and electron transfer [57]. Iordanova *et al.* [57] obtained an estimate of the mobility using the Einstein relation, and in the case of hole mobility in the basal plane direction they obtained a mobility of $8.4-9 \times 10^{-5}$ $cm^2V^{-1}s^{-1}$. This, again, is in good agreement with our results. This does not rule out the possibility of higher mobilities in doped Cr_2O_3, as the model used in Ref. [57] addresses only a Cr_2O_3 lattice where hole transfer occurs. A more disperse valence band could be achieved by introducing acceptor defects. Changing the crystal structure by doping, either by different cations introducing larger internal strain fields that can reduce the Cr-Cr hopping distance or by anionic doping directly distorting the oxygen octahedral, may positively affect the mobility. For the Cu(I)-based delafossite TCOs, the a lattice parameter (and therefore the Cu-Cu distances) influences the conductivity of the material [13]. This is related to the hopping mechanisms involved; therefore, a similar dependence should be expected for Cr_2O_3.

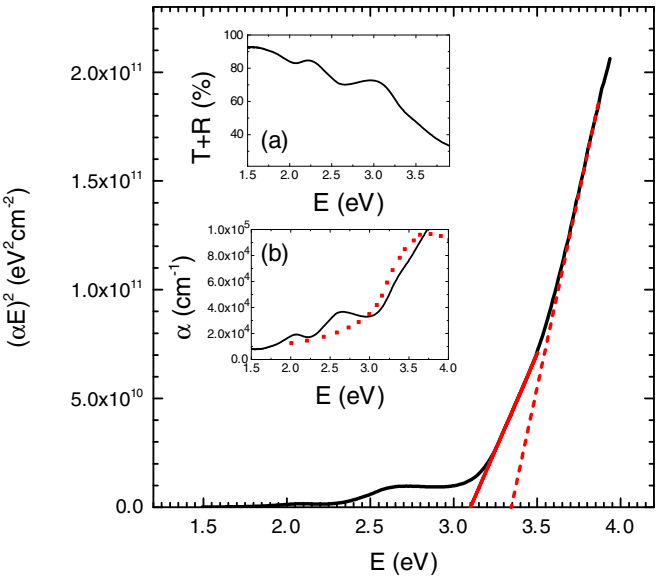

FIG. 11. (Color online) Experimental data fitted for a direct gap transition in order to obtain an estimate of the bandgap. Inset (a) shows the sum of the transmittance and reflectance as a function of energy. Inset (b) shows a comparison of the absorption coefficient of Cr_2O_3:Mg to $CuCrO_2$:Mg [62] (dotted red line).

VI. FIGURE OF MERIT

For a TCO, the optimization of both the optical and electronic properties are equally important. Hence the transmittance and reflectance of our samples were measured in order to calculate the figure of merit (FOM) as given by Eq. (10). The reflectance is included to minimize the effect of Fabry-Pérot oscillations on the evaluation of the FOM. The transmittance of our films in the visible range were all high with little variance with Mg doping. The sum of the transmittance and reflectance were in the range 70–90% for films of thicknesses 50–150 nm. Figure 11 shows a plot of $(\alpha E)^2$ vs E, where α is the absorption coefficient and E is the photon energy. The direct energy gap is estimated by fitting the linear portion of the profile and extrapolating to $\alpha = 0$ (Tauc plot). Due to the presence of absorption bands below the bandgap and deviation from the ideal square root dependence required for a Tauc plot bandgap estimate, there is a large error in determining the bandgap, as indicated by the two possible Tauc fits of the fundamental absorbance shown in Fig. 11. Our films show direct bandgaps in the 3.1–3.4 eV range for doped and undoped films. This compares reasonably with the accepted bulk value of 3.4 eV [34] and previous experimental studies [30]. Optical transitions below the bandgap arise from weak d-d^* transitions of the Cr^{3+} multiplet and are visible at 2 and 2.6 eV in the absorption spectra. The green color of bulk Cr_2O_3 is attributed to these transitions [50]. These are weak enough to not greatly reduce the transparency of the material in thin film form. α is plotted as function of energy in Fig. 11, inset (b). It is also compared to $CuCrO_2$:Mg [62]. In order to compare our films to the literature the FOM F was calculated [14],

$$F = \frac{\sigma}{\alpha} = \frac{-1}{R_{sh}\ln(T+R)}, \tag{10}$$

where R_{sh} is the sheet resistance, T is the average transmittance, and R is reflectance. The T and R values are the average of 30 points over the 1.5–3 eV range. The best FOM of 6.7 $M\Omega^{-1}$ was comparable to films previously grown by spray pyrolysis [14], 7.2 $M\Omega^{-1}$. This is the same order of magnitude as pulsed laser deposition (PLD) grown $CuAlO_2$ [63]. Typical films grown from the Cr source without postannealing have relatively low conductivity and therefore low $F(\sim 1\,M\Omega^{-1})$.

Although epitaxial films should reduce the density of structural defects and grain boundaries in comparison to spray-pyrolysis grown samples, it does not improve the conductivity as expected. Partly this is caused by the limitations in the oxygen partial pressure, but, more importantly, we have shown that the conduction is most likely limited by the SPH mechanism. This implies that further improvements of the material require growth modes using oxygen rich environments and dopants aimed to improve the polaron hopping by strain engineering rather than addressing the crystal microstructure.

VII. CONCLUSIONS

We have characterized epitaxial Mg doped Cr_2O_3 using electrical, thermoelectrical, and optical measurements. The deleterious effect of low oxygen pressure during deposition was shown, and the optimum doping range of 5–10% for the Mg/Cr ratio was identified. In poorly conductive material, we have identified a $MgCr_2O_4$-related LVM at 720 cm^{-1}, which can be suppressed by postannealing, suggesting a homogenization of the Mg content as one dominant effect from postannealing. As our experimental results are consistent with SPH, we believe the use of the model is valid. However, further work is ongoing to rule out the possibility of a band conductor. The best FOM of 6.7 $M\Omega^{-1}$ for our films does not

surpass previous work despite the epitaxial nature of our films, which is explained in terms of SPH being the limiting factor in the epitaxial material's conductivity. Thermoelectric measurements showing Seebeck coefficients in the $100-200\,\mu VK^{-1}$ range indicate that the mobility of the films are at best $1 \times 10^{-4}\,cm^2V^{-1}s^{-1}$. Such low mobilities are expected for the SPH mechanism, while an ideal p-type TCO should be a band conductor. The paper provides a clear path on how to improve the material mobility by using other growth techniques capable of higher oxygen partial pressure such as PLD or magnetron sputtering. Without further modulation of the valence band to change the conduction mechanism, or without reducing the hopping barrier by employing alternative cationic and anionic dopants, MBE grown Cr_2O_3:Mg could likely only be used in devices where carrier mobility is of no concern.

ACKNOWLEDGMENTS

Financial support by Science Foundation Ireland under Grant No. 12/IA/1264 is gratefully acknowledged. This work was supported by the Higher Education Authority under the Programme for Research in Third-Level Institutions scheme, Cycle 5. The TEM work was conducted under the framework of the INSPIRE program, funded by the Irish Government's Program for Research in Third Level Institutions, Cycle 4, National Development Plan 2007–2013. Funding support from the Irish Research Council under Grants No. GOI/PG/2013/445 and No. GOI/PG/2013/444 is also acknowledged. The authors are grateful to Dr. Clive Downing and Robert O'Connell for help with the TEM characterization. Discussions with Dr. Elisabetta Arca are also gratefully acknowledged.

[1] T. J. M. Antonio Facchinetti, *Transparent Electronics from Synthesis to Application* (Wiley, Chichester, UK, 2010).
[2] G. Thomas, Materials science: Invisible circuits, Nature **389**, 907 (1997).
[3] J. F. Wager, Transparent electronics, Science **300**, 1245 (2003).
[4] H. Kawazoe, M. Yasukawa, H. Hyodo, M. Kurita, H. Yanagi, and H. Hosono, P-type electrical conduction in transparent thin films of $CuAlO_2$, Nature **389**, 939 (1997).
[5] H. Hosono, Recent progress in transparent oxide semiconductors: Materials and device application, Thin Solid Films **515**, 6000 (2007).
[6] K. Ueda, T. Hase, H. Yanagi, H. Kawazoe, H. Hosono, H. Ohta, M. Orita, and M. Hirano, Epitaxial growth of transparent p-type conducting $CuGaO_2$ thin films on sapphire (001) substrates by pulsed laser deposition, J. Appl. Phys. **89**, 1790 (2001).
[7] N. Duan, A. W. Sleight, M. K. Jayaraj, and J. Tate, Transparent p-type conducting $CuScO_{2+x}$ films, Appl. Phys. Lett. **77**, 1325 (2000).
[8] M. Snure and A. Tiwari, $CuBO_2$: A p-type transparent oxide, Appl. Phys. Lett. **91**, 092123 (2007).
[9] R. Nagarajan, A. D. Draeseke, A. W. Sleight, and J. Tate, p-type conductivity in $CuCr_{1-x}Mg_xO_2$ films and powders, J. Appl. Phys. **89**, 8022 (2001).
[10] D. O. Scanlon, J. Buckeridge, C. R. A. Catlow, and G. W. Watson, Understanding doping anomalies in degenerate p-type semiconductor LaCuOSe, J. Mater. Chem. C **2**, 3429 (2014).
[11] N. Mansourian-Hadavi, S. Wansom, N. H. Perry, A. R. Nagaraja, T. O. Mason, L.-h. Ye, and A. J. Freeman, Transport and band structure studies of crystalline $ZnRh_2O_4$, Phys. Rev. B **81**, 075112 (2010).
[12] E. Bobeico, E. Varsano, C. Minarini, and F. Roca, P-type strontium-copper mixed oxide deposited by e-beam evaporation, Thin Solid Films **444**, 70 (2003).
[13] D. O. Scanlon and G. W. Watson, $(Cu_2S_2)(Sr_3Sc_2O_5)$-A layered, direct band gap, p-type transparent conducting oxychalcogenide: A theoretical analysis, Chem. Mater. **21**, 5435 (2009).
[14] E. Arca, K. Fleischer, and I. V. Shvets, Magnesium, nitrogen codoped Cr_2O_3: A p-type transparent conducting oxide, Appl. Phys. Lett. **99**, 111910 (2011).
[15] S. Vishal, L. Gang, Y. Yan, C. Chih-Wei, and Y. Yang, Transition metal oxides as the buffer layer for polymer photovoltaic cells, Appl. Phys. Lett. **88**, 073508 (2006).
[16] S.-Y. Park, H.-R. Kim, Y.-J. Kang, D.-H. Kim, and J.-W. Kang, Organic solar cells employing magnetron sputtered p-type nickel oxide thin film as the anode buffer layer, Sol. Energ. Mat. Sol. Cells **94**, 2332 (2010).
[17] W. Yu, L. Shen, S. Ruan, F. Meng, J. Wang, E. Zhang, and W. Chen, Performance improvement of inverted polymer solar cells thermally evaporating nickel oxide as an anode buffer layer, Sol. Energ. Mat. Sol. Cells **98**, 212 (2012).
[18] P. L. Qin, G. J. Fang, Q. He, N. H. Sun, X. Fan, Q. Zheng, F. Chen, J. W. Wan, and X. Z. Zhao, Nitrogen doped amorphous chromium oxide: Stability improvement and application for the hole-transporting layer of organic solar cells, Sol. Energ. Mat. Sol. Cells **95**, 1005 (2011).
[19] P. L. Qin, G. J. Fang, N. H. Sun, X. Fan, Q. Zheng, F. Chen, J. W. Wan, and X. Z. Zhao, Organic solar cells with p-type amorphous chromium oxide thin film as hole-transporting layer, Thin Solid Films **519**, 4334 (2011).
[20] H. Cao, X. Qiu, Y. Liang, M. Zhao, and Q. Zhu, Sol-gel synthesis and photoluminescence of p-type semiconductor Cr_2O_3 nanowires, Appl. Phys. Lett. **88**, 241112 (2006).
[21] J. H. Park and K. Natesan, Electronic transport in thermally grown Cr_2O_3, Oxid. Met. **33**, 31 (1990).
[22] A. Holt and P. Kofstad, Electrical conductivity and defect structure of Mg-doped Cr_2O_3, Solid State Ionics **100**, 201 (1997).
[23] N. Uekawa and K. Kaneko, Dopant reduction in p-type oxide films upon oxygen absorption, J. Phys. Chem. **100**, 4193 (1996).
[24] R. C. Ku and W. L. Winterbottom, Electrical conductivity in sputter-deposited chromium oxide coatings, Thin Solid Films **127**, 241 (1985).
[25] J. S. Park and H. G. Kim, Electrical conductivity and defect models of MgO-doped Cr_2O_3, J. Am. Ceram. Soc. **71**, 173 (1988).
[26] G. M. Crosbie, G. J. Tennenhouse, R. P. Tischer, and H. S. Wroblowa, Electronically conducting doped chromium oxides, J. Am. Ceram. Soc. **67**, 498 (1984).

[27] K. Hauffe and J. Block, Disorder model for a semiconductor with characteristic defect centres, taking chromium sesqui-oxide as an example, Z. Phys. Chem. **198**, 232 (1951).

[28] W. C. Hagel, Electrical conductivity of Li-substituted Cr_2O_3, J. Appl. Phys. **36**, 2586 (1965).

[29] D. Decogan and G. A. Lonergan, Carrier mobility in Cr_2O_3, J. Phys. Chem. Solids **38**, 333 (1977).

[30] C. S. Cheng, H. Gomi, and H. Sakata, Electrical and optical properties of Cr_2O_3 films prepared by chemical vapour deposition, Phys. Stat. Sol. (a)-Applied Res. **155**, 417 (1996).

[31] A. R. Nagaraja, K. H. Stone, M. F. Toney, H. W. Peng, S. Lany, and T. O. Mason, Experimental characterization of a theoretically designed candidate p-type transparent conducting oxide: Li-doped Cr_2MnO_4, Chem. Mater. **26**, 4598 (2014).

[32] H. C. Chen, E. Gartstein, and T. O. Mason, Conduction mechanism analysis for $Fe_{1-\delta}O$ and $Co_{1-\delta}O$, J. Phys. Chem. Solids **43**, 991 (1982).

[33] A. R. Nagaraja, N. H. Perry, T. O. Mason, Y. Tang, M. Grayson, T. R. Paudel, S. Lany, and A. Zunger, Band or polaron: The hole conduction mechanism in the *p*-type spinel Rh_2ZnO_4, J. Am. Ceram. Soc. **95**, 269 (2012).

[34] S. Mu, A. L. Wysocki, and K. D. Belashchenko, Effect of substitutional doping on the Néel temperature of Cr_2O_3, Phys. Rev. B **87**, 054435 (2013).

[35] M. Tabbal, S. Kahwaji, T. C. Christidis, B. Nsouli, and K. Zahraman, Pulsed laser deposition of nanostructured dichromium trioxide thin films, Thin Solid Films **515**, 1976 (2006).

[36] M. Catti, G. Sandrone, G. Valerio, and R. Dovesi, Electronic, magnetic and crystal structure of Cr_2O_3 by theoretical methods, J. Phys. Chem. Solids **57**, 1735 (1996).

[37] R. Zimmermann, P. Steiner, and S. Hafner, Electron spectroscopies and partial excitation spectra in Cr_2O_3, J. Electron Spectrosc. Relat. Phenom. **78**, 49 (1996).

[38] S. A. Chambers, Y. Liang, and Y. Gao, Noncummutative band offset at α-Cr_2O_3/α-Fe_2O_3 (0001) heterojunctions, Phys. Rev. B **61**, 13223 (2000).

[39] E. Iguchi, K. Ueda, and W. H. Jung, Conduction in $LaCoO_3$ by small-polaron hopping below room temperature, Phys. Rev. B **54**, 17431 (1996).

[40] K. Prabakar, S. K. Narayandass, and D. Mangalaraj, Dielectric and electric modulus properties of vacuum evaporated $Cd_{0.8}Zn_{0.2}Te$ thin films, Mat. Sci. Eng. B **98**, 225 (2003).

[41] B. J. Ingram, T. O. Mason, R. Asahi, K. T. Park, and A. J. Freeman, Electronic structure and small polaron hole transport of copper aluminate, Phys. Rev. B **64**, 155114 (2001).

[42] A. N. Banerjee and K. K. Chattopadhyay, Recent developments in the emerging field of crystalline p-type transparent conducting oxide thin films, Prog. Cryst. Growth Ch. **50**, 52 (2005).

[43] Z. Wang, H. S. C. O'Neill, P. Lazor, and S. K. Saxena, High pressure Raman spectroscopic study of spinel $MgCr_2O_4$, J. Phys. Chem. Solids **63**, 2057 (2002).

[44] S.-H. Shim, T. S. Duffy, R. Jeanloz, C.-S. Yoo, and V. Iota, Raman spectroscopy and x-ray diffraction of phase transitions in Cr_2O_3 to 61 GPa, Phys. Rev. B **69**, 144107 (2004).

[45] J. Mougin, N. Rosman, G. Lucazeau, and A. Galerie, *In situ* Raman monitoring of chromium oxide scale growth for stress determination, J. Raman Spectrosc. **32**, 739 (2001).

[46] P. Dera, B. Lavina, Y. Meng, and V. B. Prakapenka, Structural and electronic evolution of Cr_2O_3 on compression to 55 GPa, J. Solid State Chem. **184**, 3040 (2011).

[47] M.-Y. Su and G. Simkovich, in *Non-Stoichiometric Compounds*, NATO ASI Series Vol. 276, edited by J. Nowotny and W. Weppner (Springer, Netherlands, 1989), Chap. 7, pp. 93–113.

[48] F. Lebreau, M. M. Islam, B. Diawara, and P. Marcus, Structural, magnetic, electronic, defect, and diffusion properties of Cr_2O_3: A DFT+U study, J. Phys. Chem. C **118**, 18133 (2014).

[49] D. P. Karim and A. T. Aldred, Localized level hopping transport in La(Sr)CrO_3, Phys. Rev. B **20**, 2255 (1979).

[50] E. Arca, K. Fleischer, S. A. Krasnikov, and I. Shvets, Effect of chemical precursors on the optical and electrical properties of p-type transparent conducting Cr_2O_3:(Mg,N), J. Phys. Chem. C **117**, 21901 (2013).

[51] D. O. Scanlon and G. W. Watson, Uncovering the complex behavior of hydrogen in Cu_2O, Phys. Rev. Lett. **106**, 186403 (2011).

[52] J. Neugebauer and C. G. Van de Walle, Hydrogen in GaN: Novel aspects of a common impurity, Phys. Rev. Lett. **75**, 4452 (1995).

[53] J. I. Pankove and N. M. Johnson (eds.), *Hydrogen in Semiconductors, Semiconductors and Semimetals* (Academic Press, Boston, 1991).

[54] A. Banerjee, S. Pal, E. Rozenberg, and B. K. Chaudhuri, Adiabatic and non-adiabatic small-polaron hopping conduction in $La_{1-x}Pb_xMnO_{3+\delta}$ ($0.0 \leqslant x \leqslant 0.5$)-type oxides above the metal—semiconductor transition, J. Phys. Cond. Matter **13**, 9489 (2001).

[55] B. Zhao, T. C. Kaspar, T. C. Droubay, J. McCloy, M. E. Bowden, V. Shutthanandan, S. M. Heald, and S. A. Chambers, Electrical transport properties of Ti-doped Fe_2O_3(0001) epitaxial films, Phys. Rev. B **84**, 245325 (2011).

[56] L. Friedman and T. Holstein, Studies of polaron motion: Part III: The Hall mobility of the small polaron, Ann. Phys. **21**, 494 (1963).

[57] N. Iordanova, M. Dupuis, and K. M. Rosso, Theoretical characterization of charge transport in chromia (α-Cr_2O_3), J. Chem. Phys. **123**, 074710 (2005).

[58] Y. Wang, H. Z. Fang, C. L. Zacherl, Z. G. Mei, S. L. Shang, L. Q. Chen, P. D. Jablonski, and Z. K. Liu, First-principles lattice dynamics, thermodynamics, and elasticity of Cr_2O_3, Surface Science **606**, 1422 (2012).

[59] H. Werheit, U. Kuhlmann, B. Herstell, and W. Winkelbauer, Reliable measurement of Seebeck coefficient in semiconductors, J. Phys.: Conf. Ser. **176**, 012037 (2009).

[60] J. Tate, H. L. Ju, J. C. Moon, A. Zakutayev, A. P. Richard, J. Russell, and D. H. McIntyre, Origin of *p*-type conduction in single-crystal $CuAlO_2$, Phys. Rev. B **80**, 165206 (2009).

[61] A. J. Bosman and H. J. Vandaal, Small-polaron versus band conduction in some transition-metal oxides, Adv. Phys. **19**, 1 (1970).

[62] S. H. Lim, S. Desu, and A. C. Rastogi, Chemical spray pyrolysis deposition and characterization of p-type $CuCr_{1-x}Mg_xO_2$ transparent oxide semiconductor thin films, J. Phys. Chem. Solids **69**, 2047 (2008).

[63] H. Yanagi, S. Inoue, K. Ueda, H. Kawazoe, H. Hosono, and N. Hamada, Electronic structure and optoelectronic properties of transparent *p*-type conducting $CuAlO_2$, J. Appl. Phys. **88**, 4159 (2000).